Report

SOURCE DATA | TRANSPARENT PROCESS | OPEN ACCESS | CHECK FOR UPDATES

EMBO reports

Molecular architecture of glideosome and nuclear F-actin in *Plasmodium falciparum*

Vojtěch Pražák[1,2,3], Daven Vasishtan[1,2,3], Kay Grünewald[1,2,3,4], Ross G Douglas[5,6] & Josie L Ferreira[7]✉

Abstract

Actin-based motility is required for the transmission of malaria sporozoites. While this has been shown biochemically, filamentous actin has remained elusive and has not been directly visualised inside the parasite. Using focused ion beam milling and electron cryo-tomography, we studied dynamic actin filaments in unperturbed *Plasmodium falciparum* cells for the first time. This allowed us to dissect the assembly, path and fate of actin filaments during parasite gliding and determine a complete 3D model of F-actin within sporozoites. We observe micrometre long actin filaments, much longer than expected from in vitro studies. After their assembly at the parasite's apical end, actin filaments continue to grow as they are transported down the cell as part of the glideosome machinery, and are disassembled at the basal end in a rate-limiting step. Large pores in the IMC, constrained to the basal end, may facilitate actin exchange between the pellicular space and cytosol for recycling and maintenance of directional flow. The data also reveal striking actin bundles in the nucleus. Implications for motility and transmission are discussed.

Keywords Malaria; Plasmodium; Actin; Motility; Cryo-electron Tomography
Subject Categories Cell Adhesion, Polarity & Cytoskeleton; Microbiology, Virology & Host Pathogen Interaction
https://doi.org/10.1038/s44319-025-00415-7
Received 31 October 2024; Revised 30 January 2025; Accepted 21 February 2025
Published online: 24 March 2025

Introduction

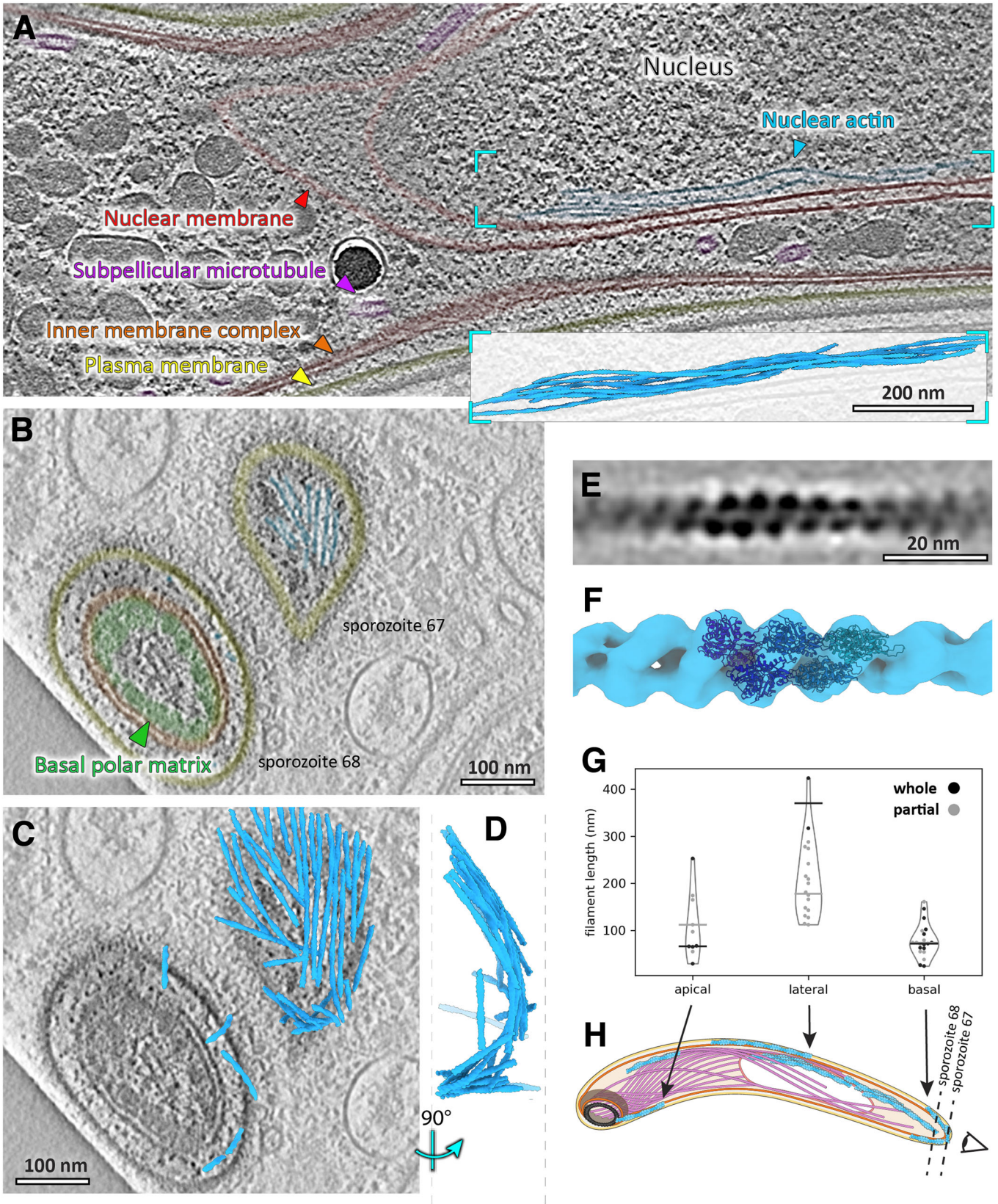
The *Plasmodium falciparum* parasite causes the most severe form of malaria in humans (Cowman et al, 2016). Infection occurs during a bite from an infected mosquito, where sporozoites leave the mosquito salivary glands and are deposited into the skin (Amino et al, 2006). Within the skin, sporozoites move rapidly (1–2 µm s^{-1}) and persistently (more than 1 h) to encounter and traverse peripheral blood capillaries. This parasite stage utilises an uncommon form of motility, termed gliding motility. It relies on a specialised, unconventional actomyosin motor system, situated below the plasma membrane, where the myosin powerstroke results in the rearward translocation of actin filaments (F-actin) and associated adhesins (Heintzelman, 2015). *Plasmodium* requires two highly sequence divergent actin isotypes for its cellular functions, with actin-1 being expressed throughout the life cycle and directly involved in gliding motility. Biochemically, actin-1 monomers assemble into F-actin at rates similar to vertebrate actin isotypes. However, *Plasmodium* F-actin appears to be dynamically unstable in vitro with very high disassembly and fragmentation rates (Schmitz et al, 2005; Vahokoski et al, 2014; Lu et al, 2019; Kumpula et al, 2017). Within the parasite, actin filaments have historically been difficult to visualise and the failure of traditional actin labelling tools on this divergent actin, has limited our understanding of dynamics within the cellular context. Recent work in *Plasmodium* and its related apicomplexan *Toxoplasma*, using the filament recognising actin chromobody, revealed localisations of actin filament pools primarily at the front (apical), rear (basal) and nuclear region of motile cells (Yee et al, 2022; Del Rosario et al, 2019; Tosetti et al, 2019). However, resolving these enigmatic actin filaments has proven difficult and an in vitro understanding of the arrangement, lengths, journey and fate of filaments in highly motile *Plasmodium* sporozoites remains unclear.

Results and discussion

We used Focused Ion Beam milling (FIB-milling) and electron cryo-tomography (cryo-ET) to image actin filaments and other subcellular structures in *Plasmodium falciparum* sporozoites (Fig. EV1). Subvolume averaging (SVA) was used to determine the structure and a complete 3D model of F-actin within sporozoites (Figs. 1 and EV2). In total, volumes corresponding to ~85 individual cells from 29 tomograms were processed. F-actin was present in all major subcellular compartments (confirmed by SVA of individual filaments/compartments, Fig. EV3): the pellicular space (the intermembrane space between the plasma membrane and the inner membrane complex and the primary site for gliding machinery), the cytosol, and most remarkably in the nucleus. Surprisingly, and unlike some previous in vitro reports (Schmitz et al, 2005; Vahokoski et al, 2014; Kumpula et al, 2017), we consistently observed actin filaments longer than 100 nm, some up to 850 nm long (Figs. 1g and EV2b). The mean length of 200 ± 140 nm (standard deviation) is likely an underestimate due to

[1]Leibniz-Institut für Virologie (LIV), Hamburg 20251, Germany. [2]Centre for Structural Systems Biology, Hamburg 22607, Germany. [3]Department of Biochemistry, University of Oxford, South Parks Road, Oxford OX1 3QU, UK. [4]Department of Chemistry, Universität Hamburg, Hamburg 20148, Germany. [5]Biochemistry and Molecular Biology, Interdisciplinary Research Centre and Molecular Infection Biology, Biomedical Research Centre Seltersberg, Justus Liebig University Giessen, Giessen 35392, Germany. [6]Institute of Veterinary Physiology and Biochemistry, Justus Liebig University Giessen, Giessen 35392, Germany. [7]Institute for Structural and Molecular Biology, Division of Biosciences, University College London, London WC1E 6BT, UK. ✉E-mail: josie.ferreira@ucl.ac.uk

 © The Author(s)


A
Nucleus
Nuclear actin
Nuclear membrane
Subpellicular microtubule
Inner membrane complex
Plasma membrane
200 nm
B
sporozoite 67
Basal polar matrix
sporozoite 68
100 nm
C
100 nm
D
90°
E
20 nm
F
G
filament length (nm)
400
300
200
100
whole
partial
apical
lateral
basal
H
sporozoite 68
sporozoite 67

© The Author(s)

Figure 1. Discrete F-actin populations are found in *P. falciparum* sporozoites.

(A) Slice through a tomogram showing a bundle of actin filaments in the nucleus. Inset shows a 3D representation of the actin bundle derived from subvolume averaging. **(B)** Slice through the basal ends of two sporozoites (see **(H)** for positioning of the slicing planes relative to the cells). **(C)** Same as **(B)** but overlaid with a 3D representation of actin from the whole tomogram. **(D)** Volume in **(C)** seen from the side. **(E)** Slice through the average volume of sporozoite F-actin. **(F)** Isosurface representation of the volume in **(E)** fitted with the molecular model of PDB 6TU4 (Vahokoski et al, 2022). **(G)** Size distribution of pellicular F-actin at different subcellular regions. Filaments that were fully contained within tomograms are shown in black, whereas those that were cut off by FIB-milling are shown in grey. Bars represent medians. $N = 48$ filaments. **(H)** Cartoon representation of a sporozoite cell with colours corresponding to structures labelled in **(A)** and dotted lines showing lamella orientations for cells 67 and 68 (~85 total) in **(B)** and **(C)**. Source data are available online for this figure.

some filaments being truncated by FIB-milling. The global F-actin concentration was measured to be 40 ± 7 μM (see Methods).

Analysis of the length distribution of pellicular F-actin shows two distinct length regulatory steps. (i) As filaments are transported down the cell towards the basal pole, they increase in length (Fig. 1G) and (ii) once at the basal pole, actin filaments are disassembled into shorter filaments (Fig. 1B–D,G). This observation of short filaments at the basal pole supports a recently proposed model of severing mediated by actin binding protein coronin, likely through recruitment of actin depolymerizing factors (ADFs) (Douglas et al, 2018), as observed for other eukaryotes. In this mechanism, initial binding by coronin to the actin filament can either shield or allow access of ADFs, thereby enhancing severing and thus filament turnover (Gandhi et al, 2009; Galkin et al, 2011; Jansen et al, 2015; Mikati et al, 2015; Ge et al, 2014). The presence of coronin at the basal end of gliding *P. berghei* sporozoites (Bane et al, 2016), the observation that coronin overexpression rescued a gliding phenotype in an actin filament stabilized sporozoite (Yee et al, 2022; Douglas et al, 2018) and the observation of shorter filaments at the basal end in comparison with middle parts of the sporozoite (this study), further suggests that such a mechanism could be employed in sporozoites. The rate of filament disassembly is slower than the rate of filament accumulation at the basal pole, and in some cases filaments accumulate at the basal pole in a one-filament deep shell, suggesting that actin disassembly may be a rate-limiting step in motility (Fig. 1B,C). Previous results from actin filament stabilisation mutants show that filament stabilisation has an influence on turnover and thus has consequences for continuous motility (Douglas et al, 2018). As actin disassembly occurs within the restricted pellicular space, a local actin monomer gradient likely forms within this space. The path of glideosome actin filaments towards the basal pole, may therefore be up an actin monomer gradient. The age of the filament together with the action of formins and this gradient could account for the elongation we observe as filaments move down the cell, prior to their disassembly at the basal pole. Localised pools of actin-stabilising proteins may also contribute to the length increase we observe.

Our data suggests that the apical and basal poles are regulatory sites for pellicular actin. At the apical pole, we observed several filaments in close proximity to the preconoidal rings (Fig. 2). Recent observations in related apicomplexans *Cryptosporidium parvum* and *Toxoplasma gondii* suggest that pellicular actin is nucleated at the preconoidal rings, implying that this is a consistent apicomplexan feature (Fig. 2A, Video 1) (Martinez et al, 2023; Dos Santos Pacheco et al, 2022). However, in *C. parvum* and *T. gondii*, the channeling of filaments into the pellicular space is dependent on extrusion of the conoid—a structural feature that is missing in *Plasmodium* sporozoites (Ferreira et al, 2023).

F-actin nucleation at the apical pole creates a constant flux of actin from the cytosol to the pellicular space. How then is the cytosolic actin pool recycled? The IMC in sporozoites has very few discontinuities, apart from the basal pole, which was dotted with ~25 nm diameter pores (Figs. 2B and EV4). These pores were observed almost exclusively at the basal end, leading us to hypothesise that their localization was related to the unusually high concentration of basal F-actin. Strikingly, we observed filamentous actin protruding through or in direct proximity to basal pores ($N = 2$), suggesting that filamentous actin can pass through (Figs. 2B and EV4C, Videos 2, 3). It is therefore possible that these pores could facilitate more efficient exchange of actin between the pellicular space and the rest of the cell. This would recycle actin and lower the concentration of actin at the rear of the sporozoite (up to 60 mM local F-actin concentration 100 nm from the basal pole end, see methods) and thus could allow for more efficient gliding. The lack of similarly sized pores at other parts of the cell indicates that their location at the basal pole is regulated, facilitating the directional flow of actin into the pellicular space only via the preconoidal rings, and into the cytoplasm only via the basal pores. This is likely a conserved apicomplexan feature as similar pores were observed in *C. parvum* (Martinez et al, 2023), while *T. gondi* has a large opening in the IMC at the basal pole—both of which could facilitate directional actin flow. It would be reasonable to speculate that the posterior/basal polar ring complex (De Niz et al, 2017) could be involved in the localisation of the pores. Notably, we have not observed a ring-like structure at the basal pole, but rather a thick amorphous layer, which we refer to as basal polar matrix (Fig. EV4C).

While examining the glideosome's local environment, we noticed a network of thin filaments reinforcing the outer IMC membrane (membrane surface pointing towards the glideosome and plasma membrane, Figs. 2C–F and 3B,C, Video 4). We refer to these filaments in *P. falciparum* as thin pellicular filaments (TPFs). TPFs were always oriented parallel to the long parasite axis, with approximately 20 nm (~5–40 nm) interfilament spacing, and with rare cross-links. A SVA of TPFs highlighted that they are embedded in the outer IMC membrane (Fig. 3C). In two cellular locations, we observed glideosomal actin filaments bound by densities consistent with myosin heads, with tails leading to TPFs in the IMC (Fig. 2F, Video 5). The observed features prompted us to hypothesise that TPFs are structural elements that allow the force generated by the glideosome to be distributed along the entire IMC. TPFs bear no ultrastructural similarity to IMC surface filaments (IMCFs) observed in *C. parvum*, which form tracks to guide actin filaments down the cell (Martinez et al, 2023). Although it has been suggested that the gliding machinery is directly connected to subpellicular microtubules (SPMTs, Harding et al, 2019), with our current approach, we see no direct connection between TPFs, actin and SPMTs through the IMC membranes (Fig. 3). Although we observe homogenous ~4 nm globular proteins that span the IMC membranes, and which we speculated may link the glideosome/TPFs to the SPMTS, these densities are not statistically associated with TPFs, indicating no interaction (Fig. 3B,D).

 © The Author(s)

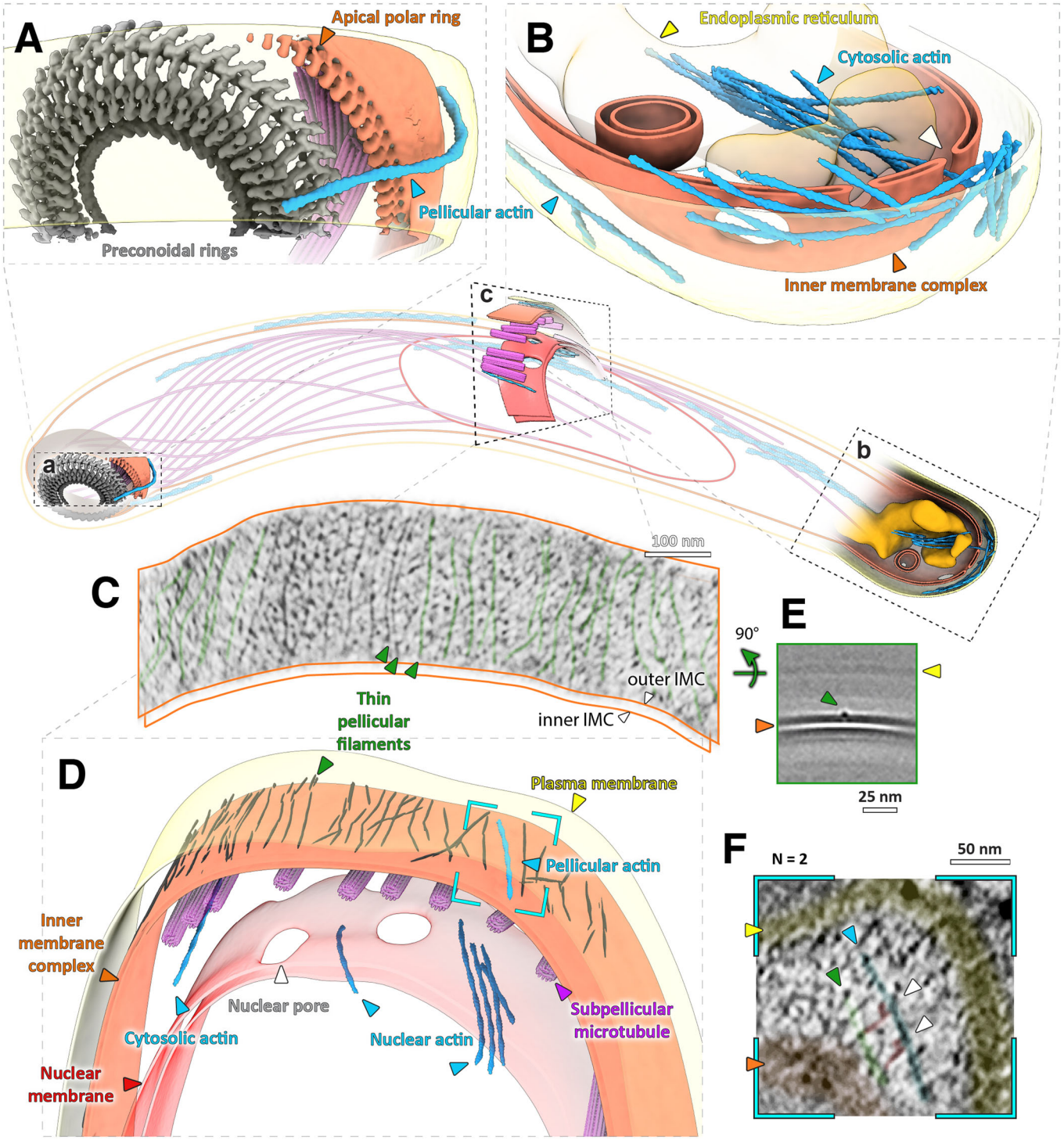
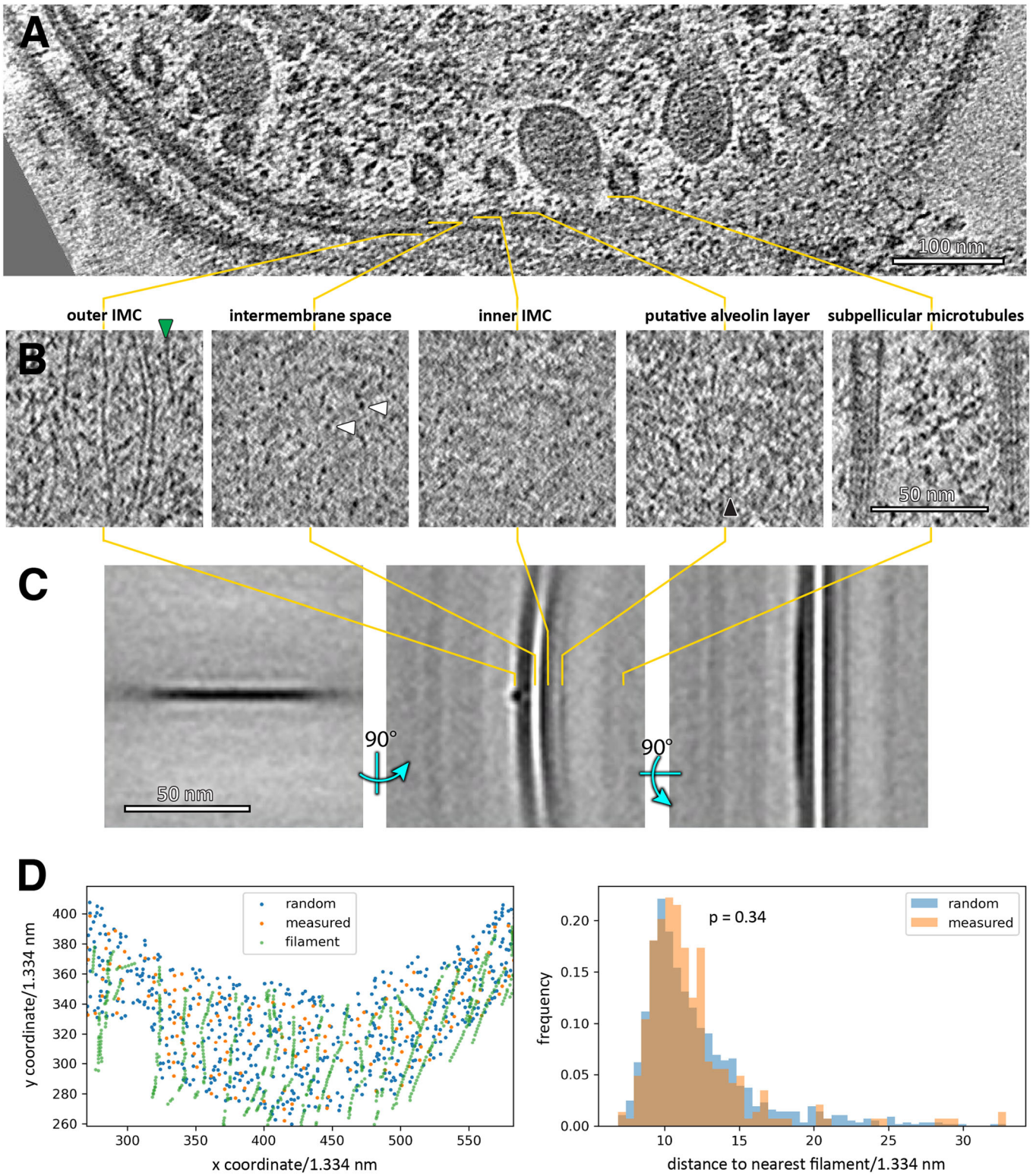


Figure 2. Visualising discrete actin populations within the 3D cellular context of motile sporozoites.

Central cartoon represents the approximate position of volumes (**A–C**) within a cell. (**A**) Apical end of showing a single actin filament being nucleated at the pre-conoidal rings (grey). (**B**) Basal end of a sporozoite, showing cytoplasmic actin bundles as well as a build-up of pellicular actin. White arrowhead indicates an actin filament going through a basal pore. Shown is also an invagination of the IMC (observed in three cells). See slice through this tomogram in Fig. EV4C. (**D**) A lateral section showing nuclear, cytosolic and pellicular F-actin. Dark lines on the outer surface of the IMC represent thin pellicular filaments (TPFs). (**C**) A slice along the surface of the outer leaflet of the outer IMC membrane. Some filaments have been highlighted in green. (**E**) A slice through the average volume of TPFs showing their position relative to the IMC membranes. Orthogonal sections through this volume also shown in Fig. 3C. (**F**) A slice through the tomogram (position shown in **D**) showing a pellicular actin filament (blue) connected to a TPF by two densities (red, white arrows) consistent with myosin dimensions (observed in two different locations). Source data are available online for this figure.

© The Author(s)



Apart from motility, F-actin is implicated in multiple cellular roles including intracellular transport, transcriptional regulation and cell structural support. We therefore analysed the populations of F-actin observed in compartments other than the pellicular space. There were numerous examples of F-actin in the cytoplasm of sporozoites (Fig. 2B,D). These were found primarily as individual filaments, with some bundles (10 separate filaments and 4 bundles consisting of 2–8 filaments). F-actin was not associated in any obvious pattern with any subcellular element, but was typically oriented along the parasite's apico-basal axis. What was most surprising was the large amounts of F-actin

 © The Author(s)

Figure 3. Analysis of the glideosome's local environment; the pellicular space.

(**A**) A slice through a tomogram (also in Fig. 2C) highlighting the pellicle ultrastructure. (**B**) Slices through tomogram shown in (**A**), oriented parallel to the inner membrane complex (IMC) at indicated relative positions. We observed a large number of globular particles spanning the space between the two IMC membranes, with a homogeneous size distribution (~4 nm diameter). (**C**) Orthogonal sections through an average volume of ~3000 thin pellicular filament particles. Middle section also shown in Fig. 2E. (**D**) We measured the distance distribution of the intermembrane particles to the nearest TPF to determine whether these may be directly interacting. However, a randomly distributed set of coordinates (on a surface defined by the measured intermembrane particle coordinates, left) has the same distribution of distances (right), indicating that no interaction takes place. Population distributions were compared using a Mann–Whitney U Test. Source data are available online for this figure.

we observed within the nucleus (Figs. 1A, 2D, Videos 4, 6, 7). In fact, the nucleus contains the majority of observed F-actin in sporozoites: approximately 60% (controlled for subcellular areas imaged in tomograms). It was found predominantly in bundles of ~3–8 filaments with at least one filament less than 10 nm from the nuclear membrane (global median distance of all filaments to the inner nuclear membrane was 21 ± 11 nm, Fig. 1A). Whether this is due to specific binding to a component of the membrane or due to marginalisation is not clear. While there have been many reports of the presence of nuclear actin in different organisms, this is to our knowledge, the first direct evidence of nuclear F-actin in the absence of staining or stabilising agents in any organism. Indeed, actin signals have indicated F-actin accumulation near to the nucleus (in ~20% of sporozoites in the case of the actin chromobody) during motility and invasion of apicomplexan parasites, suggesting that a nuclear actin cage facilitates efficient invasion and/or protects the nucleus from damage when the parasite undergoes constriction (Yee et al, 2022; Del Rosario et al, 2019; Angrisano et al, 2012). However, here we have observed extensive bundles within the nucleus itself (Figs. 1A and 2D). *Plasmodium* actin has previously been implicated in spatial repositioning of genes and histone methylation states in monoallelic expression of blood stages (Zhang et al, 2011; Volz et al, 2012). Whether these actin bundles observed in sporozoites serve as an intra-nuclear protective or mechanosensing structure, or fulfil additional molecular roles in gene expression in the nucleus requires further investigation.

Actin is key for the transmission of the malaria parasite. By dissecting the path of F-actin within the glideosome we provide new mechanistic understanding of the dynamics of filament transport down the cell, severing at the basal pole and transfer, and recycling via IMC pores. The optimal structural preservation and high resolution in situ data presented here will provide a framework for integrating future findings from other, more reductionist methods, in order to gain a complete understanding of the roles of the malaria parasite's actin cytoskeleton in motility, in the cytoplasm, and in the nucleus.

Methods

Reagents and tools table

Reagent/Resource	Reference or Source	Identifier or Catalog Number
Experimental models		
Plasmodium falciparum sporozoites	TropIQ https://tropiq.nl/	NF54-ΔPf47-5′ csp-GFP-Luc
Chemicals, Enzymes and other reagents		
L-15 Leibovitz medium	Lonza	Cat# 12-700F
RPMI – phenol red	Gibco	Cat# 11835030
UltrAufoil R1.2/1.3 300 mesh EM grids	Quantifoil https://www.quantifoil.com/products/ultraufoil	N1-A14nAu30-01
Software		
MAPS	Thermofisher scientific	
SerialEM	https://bio3d.colorado.edu/SerialEM/ Mastronarde (1997)	
IMOD	https://bio3d.colorado.edu/imod/ Kremer et al (1996)	
PEET	https://bio3d.colorado.edu/PEET/ Heumann et al (2011)	
TEMPy	https://tempy.topf-group.com/ Cragnolini et al (2021)	
Scipy	https://scipy.org/ Virtanen et al, 2020	
Scikit-learn	https://scikit-learn.org/stable/ Pedregosa et al, 2011	
Matplotlib	https://matplotlib.org/ Hunter, 2007	
Numpy	https://numpy.org/ Harris et al, 2020	
Python3	https://www.python.org/download/releases/3.0/	
Bsoft	https://cbiit.github.io/Bsoft/ Heymann, 2001	
UCSF ChimeraX	https://www.cgl.ucsf.edu/chimerax/ Pettersen et al, 2021	
Open3d	https://www.open3d.org/ preprint: Zhou et al, 2018	
Other		
Aquilos 2	Thermofisher scientific	

Obtaining sporozoites

P. falciparum sporozoites (strain: NF54-ΔPf47-5′csp-GFP-Luc: expressing a GFP-Luciferase fusion protein under the control of the csp promoter, genomic integration, no selection marker) were prepared at TropIQ (Nijmegen, Netherlands). Gametocytes were fed to 2 day old female *Anopheles stephensi* mosquitoes. Mosquito infection was confirmed 7 days post feeding by midgut dissection. At 7 days post infection, mosquitoes received an extra non-infectious blood meal to boost sporozoite production. Two weeks

© The Author(s)

post infection, sporozoites were isolated using salivary gland dissection and released using mechanical crushing into Leibovitz medium supplemented with 10% heat inactivated human serum, prior to shipping at room temperature.

Cryo-grid preparation

P. falciparum sporozoites were checked under the fluorescent microscope and then diluted 1:4 into RPMI medium (without phenol red). 3 µl of parasites were applied onto a freshly plasma-cleaned UltrAufoil R1.2/1.3 300 mesh EM grid (Quantifoil) in a humidity controlled facility. Excess liquid was manually back-blotted and grids were plunged into a reservoir of ethane/propane using a manual plunger. Grids were stored under liquid nitrogen until imaging. Two replicates were performed from independent shipments (each made up of sporozoites dissected from ~25 mosquitoes).

Cryo FIB-milling

Grids were clipped into autogrids modified for FIB preparation (Schaffer et al, 2015) and loaded into either an Aquilos or an upgraded Aquilos2 cryo-FIB/SEM dual-beam microscope (Thermofisher Scientific). Overview tile sets were recorded using MAPS software (Thermofisher Scientific) before being sputter coated with a thin layer of platinum. Good sites with parasites were identified for lamella preparation before the coincident point between the electron beam and the ion beam was determined for each point by stage tilt. Prior to milling, an organometallic platinum layer was deposited onto the grids using a GIS (gas-injection-system). Lamellae were milled manually until under 300 nm in a stepwise series of decreasing currents. Milling was performed at the lowest possible angles to increase lamella length in thin cells. Finally, polishing of all lamella was done at the end of the session as quickly as possible but always within 1.5 h to limit ice contamination from water deposition on the surface of the lamellae. Before removing the samples, the grids were sputter coated with a final thin layer of platinum. Grids were stored in liquid nitrogen for a maximum of 2 weeks before imaging in the TEM.

Tilt-series collection

Cryo-EM FIB-milled grids were rotated by 90° and loaded into a Titan Krios microscope (Thermofisher) equipped with a K3 direct electron detector and (Bio-) Quantum energy filter (Gatan). Tomographic data was collected with SerialEM with the energy-selecting slit set to 20 eV. Datasets were collected using the dose-symmetric acquisition scheme at a ±65° tilt range with 3° tilt increments. For all datasets, 5–10 frames were collected and aligned on the fly using SerialEM and the total fluence was kept to less than 120 $e^{-}Å^{2}$. Defoci between 3 and 8 µm underfocus were used to record the tilt series'.

Tomogram reconstruction

Frames were aligned on the fly in SerialEM (Mastronarde, 1997); CTF estimation, phase flipping and dose-weighting was performed in IMOD (Kremer et al, 1996). Tilt-series' were aligned in IMOD either using patch-tracking or by using nanoparticles (likely gold or platinum) on lamella surfaces as fiducial markers. Tomograms were binned 4x and filtered in IMOD or by using Bsoft (Heymann, 2001).

Subvolume averaging

Subvolume averaging was performed using PEET (Heumann et al, 2011) as described previously (Ferreira et al, 2023). Model processing was done using TEMPy (Cragnolini et al, 2021), Scipy (Virtanen et al, 2020), Scikit-learn (Pedregosa et al, 2011), Matplotlib (Hunter, 2007) and Numpy (Harris et al, 2020) in Python 3. Initial models were generated manually by picking line segments using pairs of IMOD model points and then interpolating particles at 1 voxel (1.3 nm) increments. The initial Y axes were aligned with the line segments and Y axis rotation angles were randomised. The initial reference was generated by averaging particles with the starting orientations, thus generating a featureless cylinder. A small subset of particles (~700) were refined to create a reference with F-actin features which was then used for alignment of ~70k initial positions. Duplicate and low-scoring particles were removed. In order to improve model completeness and allow separation of particles into two independent halves, the subvolume positions were then fitted to a spline-smoothed helical model allowing for small variation in helical pitch (Fig. EV2). Subvolume positions were then generated based on the best fitting model parameters. These were split into two halves and aligned independently. Overlapping particles between the two half-maps were removed before generating final half-maps. Fourier Shell Correlation was measured using Bsoft, suggesting 27 Å resolution at the 0.143 cutoff. Particles from the two half-datasets (11487 total) were then combined and aligned together. The final volume was sharpened using Bsoft with an arbitrarily chosen B-factor of −3000 for fitting and visualisation.

Segmentation and visualisation

Membrane segmentation was performed in IMOD, using drawing tools followed by linear interpolation. These were then resampled using open3d to achieve an isotropic coordinate distribution, which were then used to generate a volume using IMOD imodmop. F-actin, microtubules, apical polar ring and preconoidal rings were backplotted: average volumes were placed into 3D volumes using coordinates determined by SVA. Actin and microtubule models were smoothed for backplotting. Surface visualisation was performed using UCSF ChimeraX (Pettersen et al, 2021) or open3d (preprint: Zhou et al, 2018). Volume sections were visualised using IMOD 3dmod. Plots were generated using Matplotlib.

Length measurements

Filament lengths for comparison of nuclear, cytosolic and pellicular filament lengths were derived from helical models based on subvolume averaging positions (see above). Filament lengths for comparison of apical, lateral and basal pellicular filament lengths were measured manually using 3dmod.

Thin pellicular filament interaction analysis

To evaluate whether thin pellicular filaments (TPFs) are physically interacting with the large globular particles spanning the IMC intermembrane space, we compared their distance distribution to a random population: First, a point cloud representing the inner IMC membrane was generated using Open3d following manual

 © The Author(s)

segmentation with ~10 points per pixel. The centroid of each intermembrane particle ($N = 271$) was determined using subvolume averaging, following manual picking. These 3D coordinates (here referred to as C_{data}) were projected onto the membrane plane (via nearest neighbour) and their distance (D_{data}) to the nearest TPF particle ($N = 1333$) was measured using Scipy.spatial.KDTree. The median D_{data} was 8.3 nm. A random set of membrane coordinates (C_r) was selected to obtain an equal sample size and a similar distribution: C_{random} were no further than 11 nm from a data coordinate (mean C_{data} spacing plus two times the standard deviation). The C_{random} distance (D_{random}) to the nearest TPF was measured (8.3 nm median). D_{data} and D_{random} were compared using Mann–Whitney U Test (scipy.stats.mannwhitneyu) as the normality of both distribution differed significantly from normal when measured by scipy.stats.normaltest (p values 4.8×10^{-149} and 4.9×10^{-46}, respectively).

F-actin concentration

The number of actin subunits in observed F-actin was estimated from subvolume averaging (15,058) and manual length measurements (17,165, assuming 38 nm per 13 subunits). The subvolume averaging-derived value is likely an underestimate due to cross-correlation-based particle cleaning; it is the number of particles after the first alignment step of the two independent datasets. The two estimates were used to calculate the experimental error, expressed as standard deviation. The total observed volume of 29 tomograms with an average thickness of 244 nm was $4.2 \times 10–17$ m^3, of which cells made up approximately 7/12. 9.7×10^{-19} mol in 2.4×10^{-14} L corresponds to 4.0×10^{-5} molL^{-1}. For local actin concentration, the volume of the pellicular space was measured using manually segmented models at the basal end of a sporozoite oriented roughly perpendicularly to the FIB-sectioning axis (sporozoite 1, Fig. 1C,H). 8.73×10^{-20} moles of actin (based on subvolume averaging data) in 1.53×10^{-18} L of pellicular space corresponds to a local concentration of 5.7×10^{-2} molL^{-1} ~ 60 mM.

Data availability

Subvolume average has been deposited on the EMDB (EMD-19898): https://www.ebi.ac.uk/emdb/EMD-19898.

The source data of this paper are collected in the following database record: biostudies:S-SCDT-10_1038-S44319-025-00415-7.

Expanded view data, supplementary information, appendices are available for this paper at https://doi.org/10.1038/s44319-025-00415-7.

Peer review information

A peer review file is available at https://doi.org/10.1038/s44319-025-00415-7

References

Amino R, Thiberge S, Martin B, Celli S, Shorte S, Frischknecht F, Ménard R (2006) Quantitative imaging of Plasmodium transmission from mosquito to mammal. Nat Med 12:220–224

Angrisano F, Riglar D, Sturm A, Volz J, Delves M, Zuccala E, Turnbull L, Dekiwadia C, Olshina M, Marapana D et al (2012) Spatial localisation of actin filaments across developmental stages of the malaria parasite. PloS ONE 7:e32188

Bane KS, Lepper S, Kehrer J, Sattler JM, Singer M, Reinig M, Klug D, Heiss K, Baum J, Mueller A-K et al (2016) The actin filament-binding protein coronin regulates motility in Plasmodium sporozoites. PLOS Pathog 12:e1005710

Cowman AF, Healer J, Marapana D, Marsh K (2016) Malaria: biology and disease. Cell 167:610–624

Cragnolini T, Sahota H, Joseph AP, Sweeney A, Malhotra S, Vasishtan D, Topf M (2021) TEMPy2: a Python library with improved 3D electron microscopy density-fitting and validation workflows. Acta Crystallogr Sect Struct Biol 77:41–47

De Niz M, Burda P-C, Kaiser G, del Portillo HA, Spielmann T, Frischknecht F, Heussler VT (2017) Progress in imaging methods: insights gained into Plasmodium biology. Nat Rev Microbiol 15:37–54

Del Rosario M, Periz J, Pavlou G, Lyth O, Latorre-Barragan F, Das S, Pall GS, Stortz JF, Lemgruber L, Whitelaw JA et al (2019) Apicomplexan F-actin is required for efficient nuclear entry during host cell invasion. EMBO Rep 20:e48896

Dos Santos Pacheco N, Brusini L, Haase R, Tosetti N, Maco B, Brochet M, Vadas O, Soldati-Favre D (2022) Conoid extrusion regulates glideosome assembly to control motility and invasion in Apicomplexa. Nat Microbiol 7:1777–1790

Douglas RG, Nandekar P, Aktories J-E, Kumar H, Weber R, Sattler JM, Singer M, Lepper S, Sadiq SK, Wade RC et al (2018) Inter-subunit interactions drive divergent dynamics in mammalian and Plasmodium actin filaments. PLOS Biol 16:e2005345

Ferreira JL, Pražák V, Vasishtan D, Siggel M, Hentzschel F, Binder AM, Pietsch E, Kosinski J, Frischknecht F, Gilberger TW et al (2023) Variable microtubule architecture in the malaria parasite. Nat Commun 14:1216

Galkin VE, Orlova A, Kudryashov DS, Solodukhin A, Reisler E, Schröder GF, Egelman EH (2011) Remodeling of actin filaments by ADF/cofilin proteins. Proc Natl Acad Sci USA 108:20568–20572

Gandhi M, Achard V, Blanchoin L, Goode BL (2009) Coronin switches roles in actin disassembly depending on the nucleotide state of actin. Mol Cell 34:364–374

Ge P, Durer ZAO, Kudryashov D, Zhou ZH, Reisler E (2014) CryoEM reveals different coronin binding modes for ADP- and ADP-BeFx- actin filaments. Nat Struct Mol Biol 21:1075

Harding CR, Gow M, Kang JH, Shortt E, Manalis SR, Meissner M, Lourido S (2019) Alveolar proteins stabilize cortical microtubules in Toxoplasma gondii. Nat Commun 10:401

Harris, Millman CR, van der Walt KJ, Gommers R SJ, Virtanen P, Cournapeau D, Wieser E, Taylor J, Berg S, Smith NJ et al (2020) Array programming with NumPy. Nature 585:357–362

Heintzelman MB (2015) Gliding motility in apicomplexan parasites. Semin Cell Dev Biol 46:135–142

Heumann JM, Hoenger A, Mastronarde DN (2011) Clustering and variance maps for cryo-electron tomography using wedge-masked differences. J Struct Biol 175:288–299

Heymann JB (2001) Bsoft: image and molecular processing in electron microscopy. J Struct Biol 133:156–169

Hunter JD (2007) Matplotlib: a 2D graphics environment. Comput Sci Eng 9:90–95

Jansen S, Collins A, Chin SM, Ydenberg CA, Gelles J, Goode BL (2015) Single-molecule imaging of a three-component ordered actin disassembly mechanism. Nat Commun 6:7202

Kremer JR, Mastronarde DN, McIntosh JR (1996) Computer visualization of three-dimensional image data using IMOD. J Struct Biol 116:71–76

© The Author(s)

Kumpula E-P, Pires I, Lasiwa D, Piirainen H, Bergmann U, Vahokoski J, Kursula I (2017) Apicomplexan actin polymerization depends on nucleation. Sci Rep 7:12137

Lu H, Fagnant PM, Trybus KM (2019) Unusual dynamics of the divergent malaria parasite PfAct1 actin filament. Proc Natl Acad Sci USA 116:20418–20427

Martinez M, Mageswaran SK, Guérin A, Chen WD, Thompson CP, Chavin S, Soldati-Favre D, Striepen B, Chang Y-W (2023) Origin and arrangement of actin filaments for gliding motility in apicomplexan parasites revealed by cryo-electron tomography. Nat Commun 14:4800

Mastronarde DN (1997) Dual-axis tomography: an approach with alignment methods that preserve resolution. J Struct Biol 120:343–352

Mikati MA, Breitsprecher D, Jansen S, Reisler E, Goode BL (2015) Coronin enhances actin filament severing by recruiting cofilin to filament sides and altering F-actin conformation. J Mol Biol 427:3137

Pedregosa F, Varoquaux G, Gramfort A, Michel V, Thirion B, Grisel O, Blondel M, Prettenhofer P, Weiss R, Dubourg V et al (2011) Scikit-learn: Machine Learning in Python. J Mach Learn Res 12:2825-2830

Pettersen EF, Goddard TD, Huang CC, Meng EC, Couch GS, Croll TI, Morris JH, Ferrin TE (2021) UCSF ChimeraX: structure visualization for researchers, educators, and developers. Protein Sci 30:70–82

Schaffer M, Engel BD, Laugks T, Mahamid J, Plitzko JM, Baumeister W (2015) Cryo-focused ion beam sample preparation for imaging vitreous cells by cryo-electron tomography. Bio-Protoc 5:e1575

Schmitz S, Grainger M, Howell S, Calder LJ, Gaeb M, Pinder JC, Holder AA, Veigel C (2005) Malaria parasite actin filaments are very short. J Mol Biol 349:113–125

Tosetti N, Dos Santos Pacheco N, Soldati-Favre D, Jacot D (2019) Three F-actin assembly centers regulate organelle inheritance, cell-cell communication and motility in Toxoplasma gondii. eLife 8:e42669

Vahokoski J, Bhargav SP, Desfosses A, Andreadaki M, Kumpula E-P, Martinez SM, Ignatev A, Lepper S, Frischknecht F, Sidén-Kiamos I et al (2014) Structural differences explain diverse functions of Plasmodium actins. PLoS Pathog 10:e1004091

Vahokoski J, Calder LJ, Lopez AJ, Molloy JE, Kursula I, Rosenthal PB (2022) High-resolution structures of malaria parasite actomyosin and actin filaments. PLOS Pathog 18:e1010408

Virtanen P, Gommers R, Oliphant TE, Haberland M, Reddy T, Cournapeau D, Burovski E, Peterson P, Weckesser W, Bright J et al (2020) SciPy 1.0: fundamental algorithms for scientific computing in Python. Nat Methods 17:261–272

Volz JC, Bártfai R, Petter M, Langer C, Josling GA, Tsuboi T, Schwach F, Baum J, Rayner JC, Stunnenberg HG et al (2012) PfSET10, a Plasmodium falciparum methyltransferase, maintains the active var gene in a poised state during parasite division. Cell Host Microbe 11:7–18

Yee M, Walther T, Frischknecht F, Douglas RG (2022) Divergent Plasmodium actin residues are essential for filament localization, mosquito salivary gland invasion and malaria transmission. PLOS Pathog 18:e1010779

Zhang Q, Huang Y, Zhang Y, Fang X, Claes A, Duchateau M, Namane A, Lopez-Rubio J-J, Pan W, Scherf A (2011) A critical role of perinuclear filamentous actin in spatial repositioning and mutually exclusive expression of virulence genes in malaria parasites. Cell Host Microbe 10:451

Zhou Q-Y, Park J, Koltun V (2018) Open3D: a modern library for 3D data processing. Preprint at https://arxiv.org/abs/1801.09847

Acknowledgements

We thank Lindsay Baker for helpful discussions and Carolyn Moores for her continued support and critical reading of the manuscript. Thank you to the CSSB EM facility team for their support; this research was funded in part by DFG INST 152/ 772-1, 774-1, 775-1, 777-1 FUGG (CSSB cryoEM facility). We gratefully acknowledge funding by HFSP long-term postdoctoral fellowship LT000024/2020-L (JLF), Infrastructures for the control of vector-borne diseases (Infravec2) funded by the EU's Horizon 2020 programme (grant agreement No 731060) (JLF), Wellcome Career Development award 227774/Z/23/Z (JLF), LOEWE Centre DRUID ("Novel Drugs Targets against Poverty-related and Neglected Tropical Infectious Diseases") within the Hessian Excellence Program (RGD). Wellcome Trust 209250/Z/17/ Z and 107806/Z/15/Z (KG). For the purpose of open access, the author has applied a Creative Commons Attribution (CC BY) licence to any Author Accepted Manuscript version arising.

Author contributions

Vojtech Pražák: Conceptualization; Data curation; Software; Formal analysis; Validation; Investigation; Visualization; Methodology; Writing—original draft; Writing—review and editing. **Daven Vasishtan**: Software; Validation. **Kay Grünewald**: Resources; Supervision; Funding acquisition; Writing—review and editing. **Ross G Douglas**: Conceptualization; Data curation; Writing—original draft; Writing—review and editing. **Josie L Ferreira**: Conceptualization; Funding acquisition; Validation; Investigation; Methodology; Writing—original draft; Project administration; Writing—review and editing.

Source data underlying figure panels in this paper may have individual authorship assigned. Where available, figure panel/source data authorship is listed in the following database record: biostudies:S-SCDT-10_1038-S44319-025-00415-7.

Disclosure and competing interests statement

The authors declare no competing interests.

Open Access This article is licensed under a Creative Commons Attribution 4.0 International License, which permits use, sharing, adaptation, distribution and reproduction in any medium or format, as long as you give appropriate credit to the original author(s) and the source, provide a link to the Creative Commons licence, and indicate if changes were made. The images or other third party material in this article are included in the article's Creative Commons licence, unless indicated otherwise in a credit line to the material. If material is not included in the article's Creative Commons licence and your intended use is not permitted by statutory regulation or exceeds the permitted use, you will need to obtain permission directly from the copyright holder. To view a copy of this licence, visit http://creativecommons.org/licenses/by/4.0/. Creative Commons Public Domain Dedication waiver http://creativecommons.org/publicdomain/zero/1.0/ applies to the data associated with this article, unless otherwise stated in a credit line to the data, but does not extend to the graphical or creative elements of illustrations, charts, or figures. This waiver removes legal barriers to the re-use and mining of research data. According to standard scholarly practice, it is recommended to provide appropriate citation and attribution whenever technically possible.

© The Author(s) 2025

Expanded View Figures

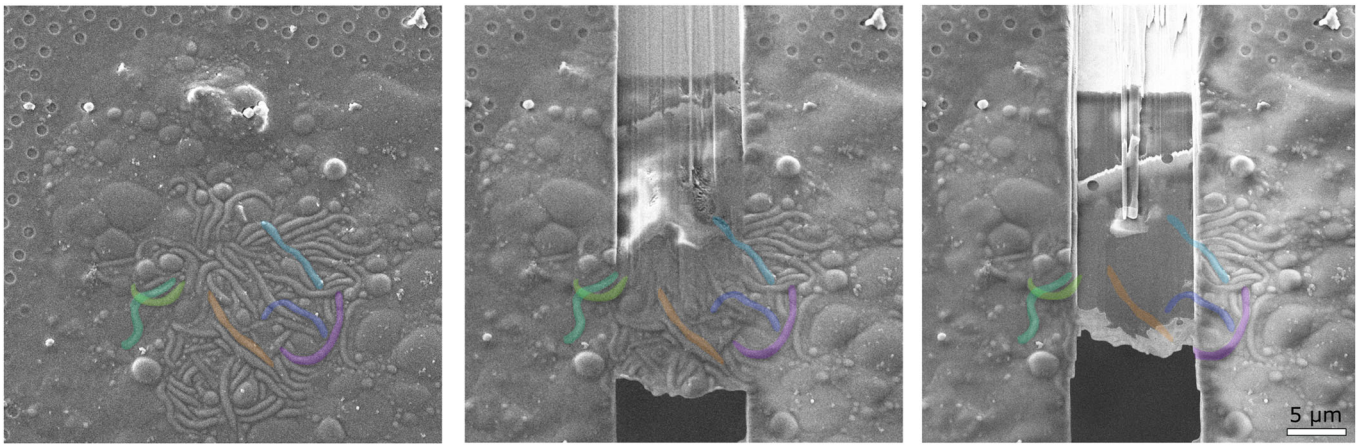


Figure EV1. FIB-milling sporozoites.

Left: A pile of sporozoites in the SEM. A few individual sporozoites are coloured consistently in all three images. Middle: SEM image during the FIB-milling process. Right: SEM image of the final polished lamella. Source data are available online for this figure.

© The Author(s)

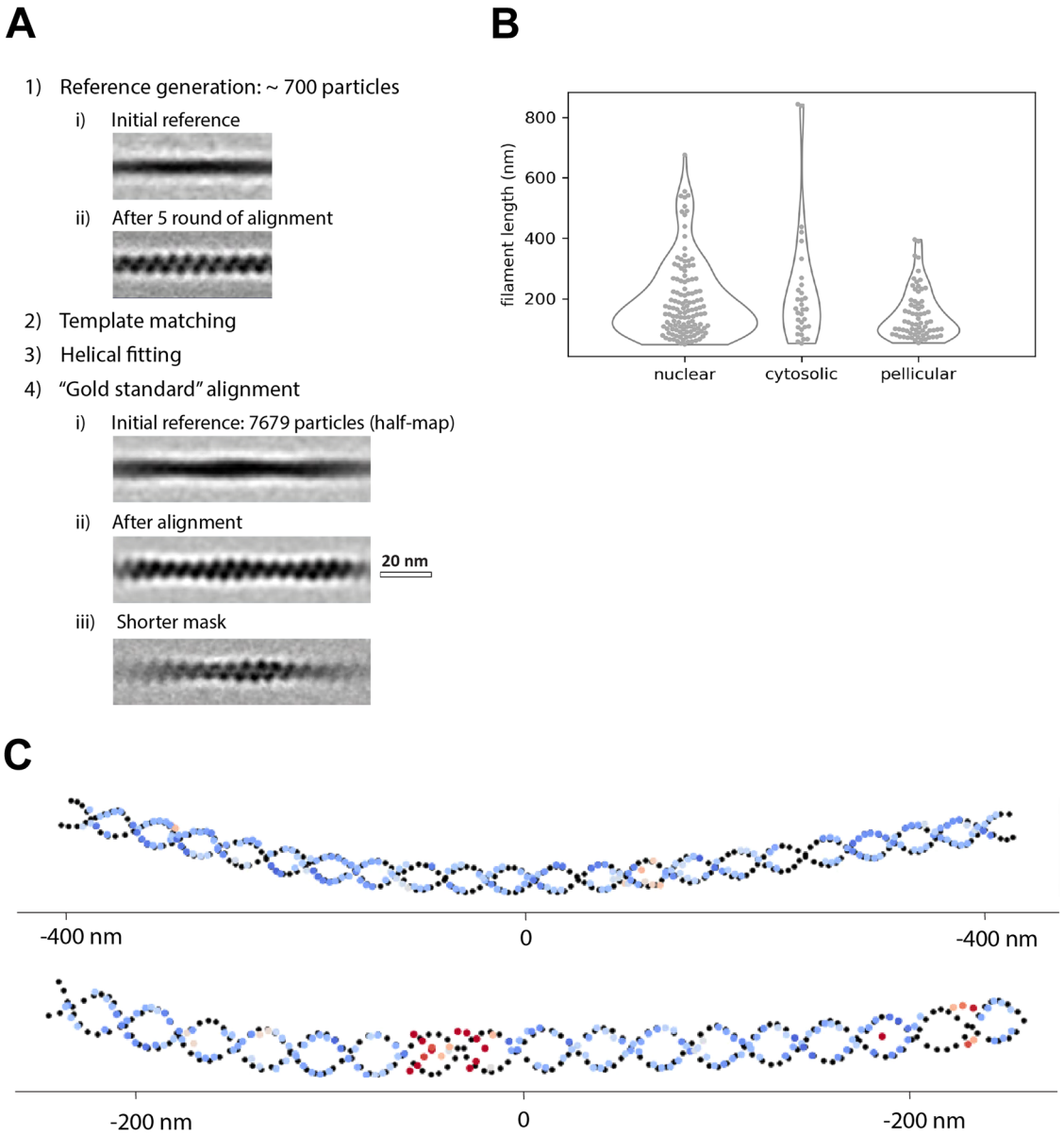


Figure EV2. Subvolume averaging of actin.

(**A**) A rough outline of the workflow used for subvolume averaging of actin, with some reference volumes shown. (**B**) Size distribution of F-actin in indicated subcellular locations derived from subvolume averaging coordinates. Note that especially longer filaments were frequently truncated during FIB-milling causing the distribution to be skewed towards shorter sizes. Two-sided t-test *p*-values are 0.4 and 1×10^{-4} comparing nuclear and cytosolic, and nuclear and pellicular, respectively. Caution should be used interpreting the significance of the difference due to some filaments being truncated. (**C**) Diagnostic plots of helical fitting of two longer filaments. Black dots show best fit positions of actin subunits. Overlaid are positions measured by subvolume averaging coloured from blue to red based on distance to the nearest model point. Source data are available online for this figure.

 © The Author(s)

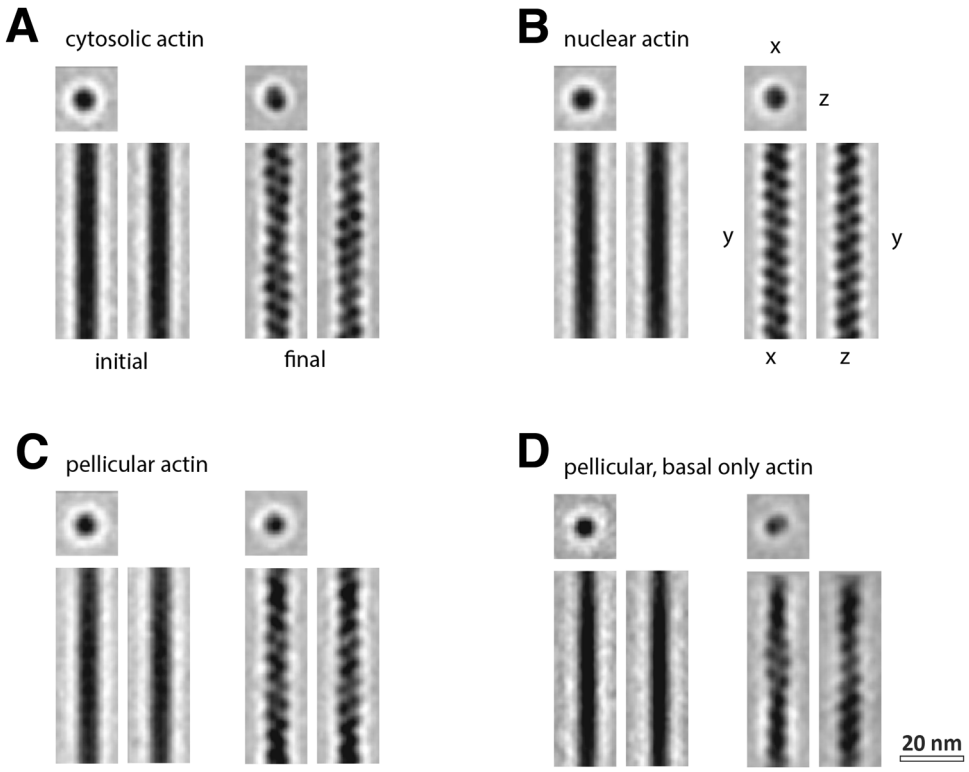


Figure EV3. Subvolume averages of actin from different subcellular compartments.

Actin filaments used for subvolume averaging (Figs. 1E and EV2) were manually split into classes based on their subcellular localization: (**A**) cytosol, (**B**) nucleus, (**C**) pellicular space, (**D**) pellicular space at the basal end. The particle Y axis (long filament axis) orientations were randomised and independent references were generated for each class (left hand side). Alignment was performed without refining orientations. Source data are available online for this figure.

© The Author(s)

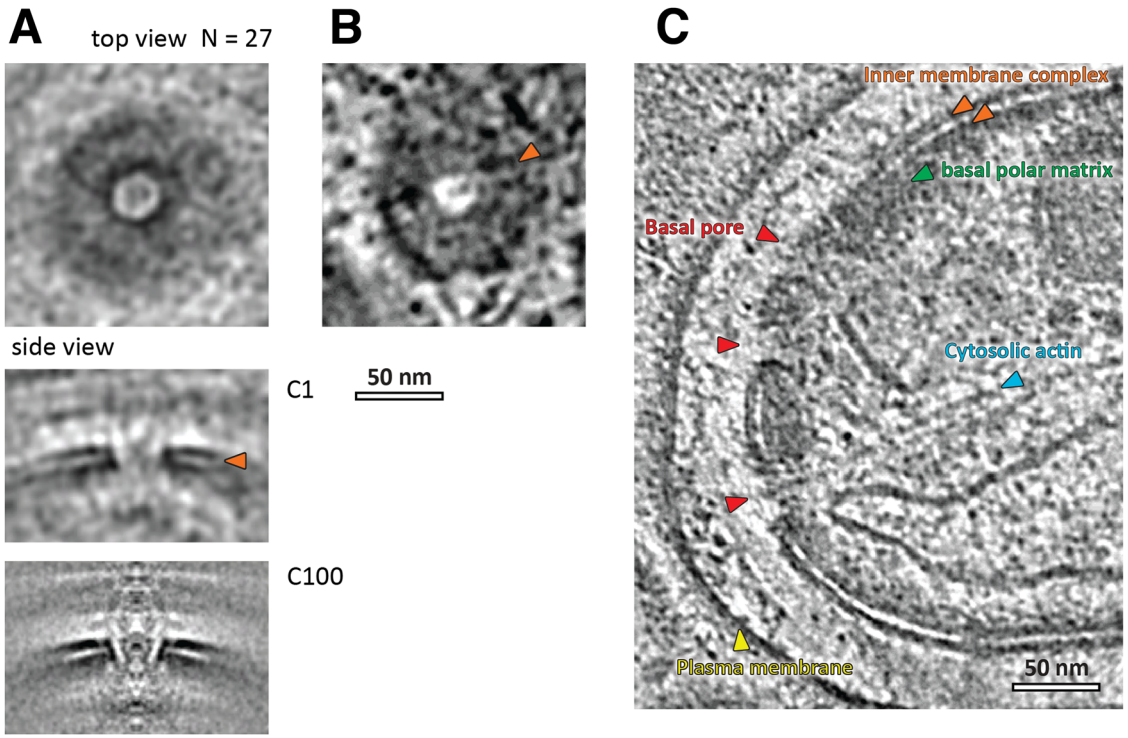


Figure EV4. Basal pores form 25 nm diameter connections between the cytoplasm and pellicular space.

(**A**) Subvolume average of 27 particles. No symmetry is evident at this resolution. (**B**) A tangential slice through a single pore. (**C**) Slice through a basal end of a sporozoite (also in Fig. 2B) showing three basal pores. Source data are available online for this figure.

 © The Author(s)